Atmospheric inverse estimates of CO emissions from Zhengzhou, China

Hao Fan [a], Chuanfeng Zhao [a, *], Zhanshan Ma [a, b], Yikun Yang [a]

[a] *State Key Laboratory of Earth Surface Processes and Resource Ecology, and College of Global Change and Earth System Science, Beijing Normal University, Beijing 100875, China*
[b] *National Meteorological Center, Beijing, China*

ARTICLE INFO

ABSTRACT

Carbon monoxide (CO) is an important gas that affects human health and causes air pollution. However, the estimates of CO emissions in China are still subject to large uncertainties. Based on the CO mass concentration and the coupled Weather Research and Forecast (WRF) and Stochastic Time-Inverted Lagrangian Transport (STILT) model (WRF-STILT), this study estimates the CO emissions over Zhengzhou, China. The results show that the mean CO mass concentration was 1.17 mg m^{-3} from November 2017 to February 2018, with a clear diurnal variation. There were two periods of rapidly increasing CO concentration in the diurnal variation, which are 06:00–09:00 and 16:00–20:00 local time. The footprint analysis shows that the observation site is highly influenced by local emissions. The most influential regions to the site observations are northeast and northwest Zhengzhou, which are associated with the geographical barrier of the Taihang Mountains in the north and narrow Fenwei Plain in the west. The inversion result shows that the actual emissions are lower than the inventory estimates. Using the optimal scaling factors, the WRF-STILT simulations of CO concentration agree closely with the CO measurements with the linear fitting regression equation $y = 0.87x + 0.15$. The slopes of the linear fitting regressions between the WRF-STILT-simulated CO concentrations determined using the optimal emissions and the observations range from 0.72 to 0.89 for four months, and all the fitting results passed the significance test (P < 0.001). These results indicate that the new optimal emissions derived with the scaling factors could better represent the real emission conditions than the *a priori* emissions if the WRF-STILT model is assumed to be reliable.

© 2020 Elsevier Ltd. All rights reserved.

1. Introduction

Carbon monoxide (CO) is a major pollutant in the troposphere and an important gas in the global carbon cycle (Holloway et al., 2000; Li and Liu, 2011; Streets et al., 2006). CO is a colourless, odourless gas with a long life cycle of approximately 2–3 months (Liu et al., 2019a,b; Stocker et al., 2013). In general, exposure to an environment with a CO concentration of 10 ppm or higher can reduce the oxygen transmission of human cells and can endanger life (Liu et al., 2018a; Singh et al., 2016; Townsend and Maynard, 2002; Vandyck et al., 2018; WHO, 1999). Moreover, CO plays a central role in atmospheric chemistry by acting as the largest sink of hydroxyl radicals and by being involved in the production of ozone (Choi et al., 2017; Petetin et al., 2018).

CO is one of the main air pollutants in China (Kang et al., 2019; Li and Liu, 2011; Wang et al., 2018). The production of CO is mainly from natural sources and anthropogenic sources, such as the oxidation of methane in the atmosphere, incomplete combustion of carbon fuels, and emissions from the ocean (Hernández-Paniagua et al., 2018; Jiang et al., 2015a; Jiang et al., 2015b; WHO, 1999). In large cities, the main sources of CO are industry, transportation, and boiler heating (Che et al., 2016; Marey et al., 2015; Yue et al., 2018). Note that the increase in CO can promote the production of CO_2 and ozone (Feng et al., 2020; Girach et al., 2017). CO is generally stable in air, and its diffusion and migration are mainly controlled by the wind and can be transported over long distances by the airflow (Garrett et al., 2010; Dekker et al., 2017; Dekker et al., 2019; Jiang et al., 2017; Khan et al., 2017).

Compared to the number of studies on other air pollutants, there have been relatively few studies (Liu et al., 2019b; Pal et al., 2017;

---

* Corresponding author.
  E-mail address: czhao@bnu.edu.cn (C. Zhao).

Yin et al., 2015) on CO worldwide, especially in China. Previous CO studies have mainly focused on statistical analyses of the spatial and temporal distributions of various air pollutants including CO using ground monitoring data, remote sensing data or emission inventory products (Kang et al., 2019; Saikawa et al., 2017; Sun et al., 2018; Yue et al., 2018; Zheng et al., 2014). In terms of predicting CO concentration from models, existing studies (Dekker et al., 2017; Jiang et al., 2015a; Zheng et al., 2014) generally derive it based on air quality models along with an *a priori* emission map. However, *a priori* emission information is generally obtained from emission inventories, which have limited time resolution and large uncertainties due to various influential factors, such as differences in air pollutant emission coefficients and complex sources of pollution emissions (Hassler et al., 2016; Saikawa et al., 2017; Streets et al., 2006). At the same time, the lack of long-term and continuous ground observations increases the difficulty of assessing inventory model performance (Hu et al., 2019; Jeong et al., 2012a; Zhao et al., 2009).

Using ground site observations and inversion simulation, this study provides an independent method to quantify CO emissions. To date, the use of the Stochastic Time-Inverted Lagrangian Transport (STILT) model to track the transport of particles in the atmosphere has been successfully and widely applied (Hu et al., 2018; Hu et al., 2019; Jeong et al., 2012a; Mallia et al., 2015; Nehrkorn et al., 2010; Zhao et al., 2009). In the United States, California has the strongest greenhouse gas emissions among all states, and the STILT model is often used to track pollution and greenhouse gas emissions there (Brophy et al., 2019; Cui et al., 2019; Jeong et al., 2012a,b; Zhao et al., 2009). Existing researches suggest that an atmospheric inversion model requires a sufficient amount of CO concentration data, an *a priori* CO emission map, footprint data for CO predictions, and meteorology data for driving the transport model (Jeong et al., 2016; Lin et al., 2003; Zhao et al., 2009).

Central China is one of the heavily air-polluted areas in China (Liu et al., 2019b; Zheng et al., 2018). One goal of the government is to reduce the rapid growth of CO in autumn and winter to improve air quality. To meet this goal, we need to clearly know the emissions of CO over different regions. In this paper, we use the Weather Research and Forecast (WRF) coupled with the STILT model (WRF-STILT) and site CO concentration measurements to estimate the CO emissions in Zhengzhou and the surrounding areas. The WRF-STILT model provides both accurate meteorological field simulations from WRF and convenient footprint simulations from STILT (Lin et al., 2003; Nehrkorn et al., 2010; Zhao et al., 2009), which are suitable for studying the physical transport mechanism and diffusion effect of CO. With the footprints from WRF-STILT, we then use the least square inversion technique to obtain the scaling factors for optimal emission estimation. After obtaining optimal emission information, we conduct an evaluation test by comparing the CO concentration from the ground observations and that from the new emission-based model predictions.

2. Data and method

2.1. Study area

Fig. 1 shows the location of our study area, including Zhengzhou and its surrounding area. Zhengzhou is the capital of Henan Province and a major industrial city in central China, with a population of more than 10 million. It is located from the intersection of the middle and lower reaches of the Yellow River to the Huanghuai Plain. As shown in Fig. 1, the terrain is high in the west (over 1000 m), low in the east (roughly between 100 m and 300 m), and the Taihang Mountains are in the north of this area. This terrain affects the transport of air pollutants (Liu et al., 2018a,b; Wang et al.,

2018). As of 2018, Zhengzhou has jurisdiction over six municipal districts, one county and five county-level cities, with a total area of 7446 square kilometres, a built-up area of 830.97 square kilometres, and a total population of 10.13 million. The total production value is 1014.33 billion yuan (CSY, 2018). Zhengzhou is the central city of the Central Plains urban agglomeration. In recent years, with rapid economic development and large-scale air pollution, the environment in Zhengzhou and its surrounding areas has been greatly affected (Liu et al., 2018b). CO is a common polluted gas in the region, especially in autumn and winter; this CO not only destroys the natural environment but also causes great harm to human health. A quantitative assessment of CO concentration and CO emissions over this area is necessary. We divide the Zhengzhou area into 10 sub-regions, as shown in Fig. 5, based on the spatial distribution of the *a priori* CO emissions, although the region classification is somehow subjective. These 10 sub-regions are used in the following analysis.

2.2. Measurements

The CO concentration measurements were obtained for the period from November 1, 2017, to February 28, 2018, at a site located in the centre of Zhengzhou (latitude and longitude of $34.75°$ N and $113.60°$ E), as shown by the star in Fig. 1. The site observations are operated by the Ministry of Ecology and Environment of the People's Republic of China, which are released on the website (http://www.mee.gov.cn/) of the China Ministry of Ecology and Environment (MEE) in real-time.

The CO sensor was a 48i CO analyser from Thermo Fisher Scientific (USA). The important parameters are as follows: the custom range is $0.1-10,000$ (ppm or mg/m^3), the zero noise is 0.02 ppm RMS (30 s averaging time), the lower detectable limit is 0.04 ppm, the zero drift (24 h) is < 0.1 ppm, the sample flow rate is 1 L/min, the response time is 60 s (30 s average time), the span drift is ±1% full scale, and the linearity is ±1% full scale (https://www.thermofisher.com/order/catalog/product/48I#/48I). The MEE has established strict standards to ensure the data quality, such as maintaining the zero noise ≤0.25 ppm, zero drift within ±0.1 ppm, the lower detectable limit ≤0.05 ppm, the indication error within ±2%, the response time ≤4 min, and the range precision ≤0.05 ppm. When these conditions are met and the sampling time is at least 45 min per hour, MEE calculates and provides hourly data. By choosing the observation period from November 1, 2017, to February 28, 2018, we focus on the estimation of CO emissions in Zhengzhou during winter. Note that the original hourly CO mass concentration data with a quality flag of "good" are used in this study. The quality check was performed by the MEE, and a "good" flag was given when there were no missing data, when no outliers appeared, and when no instrument error occurred.

2.3. The a priori CO emission map

In this study, the monthly *a priori* CO emission map (F) is obtained from the Multiresolution Emission Inventory for China (MEIC) developed by Tsinghua University. The MEIC includes a set of anthropogenic emissions inventory models for air pollutants and greenhouse gases developed in China based on cloud computing platforms. It is more suitable for investigating China's energy statistics than other emission inventories are and is able to demonstrate CO emission changes month by month (Fan et al., 2018), which is beneficial for the *a priori* emission map in this study. The spatial resolution for the CO emission map is $0.25° \times 0.25°$. A detailed description of the MEIC can be found on the official website (http://www.meicmodel.org) and in previous studies (Li et al., 2014; Liu et al., 2015; Zhang et al., 2009; Zheng et al., 2014) and
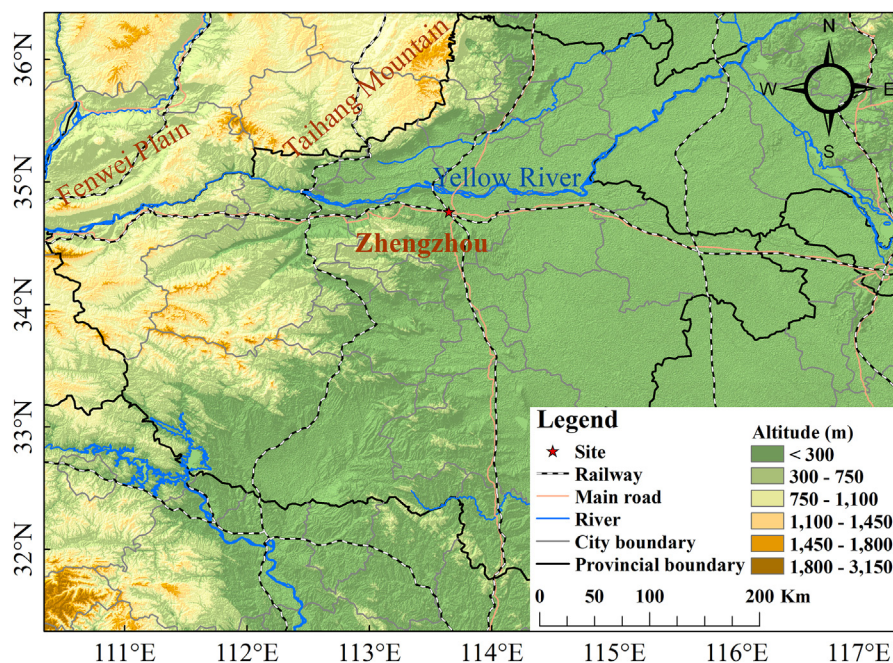
Fig. 1. Location of the study area. The site is marked with a star.

is not repeated here.

2.4. WRF-STILT model

The WRF-STILT model is widely used for the study of the transport of atmospheric gases, including both polluted gases and greenhouse gases. As an atmospheric backward transport model, it can directly obtain the contribution rate of emissions over different regions in the study area from the measurements at a fixed location based on the simulated footprint (Cusworth et al., 2018; Wen et al., 2012; Wu et al., 2018). The first novelty of this coupled model is that it reduces the transport error in the top-down greenhouse gas flux estimation at the continental scale, specializing in regional emission simulation and flux inversion of greenhouse gases (Nehrkorn et al., 2010; Zhao et al., 2009). The details of the WRF-STILT model have been described in previous studies (Lin et al., 2003; Nehrkorn et al., 2010). Here, we only describe the features and settings most relevant to this study.

The initial and boundary meteorological conditions for the WRF are set up based on the National Centre for Environmental Prediction final analysis data. The simulation domain is 900 km × 900 km, with a horizontal resolution of 3 km. Similar to our previous model setup (Zhao et al., 2009; Zhao et al., 2019), the main physical modules of the WRF operation are set as follows. The longwave radiation uses the Rapid Radiation Transfer Model scheme, and the shortwave radiation uses the Goddard radiation transfer model scheme; the boundary layer uses the Yonsei University scheme; the microphysical module uses the Purdue Lin module; and the convection uses the Grell-Devenyi ensemble mass flux scheme. For the STILT setup, a release height of 10 m at the observation station is used to represent the receptor location of CO measurements in the study area. As a national environment station, there are no local CO emission sources nearby within approximately 0.5 km. Thus, the CO concentration at the receptor location is weakly subject to local enhancement by nearby sources that are not represented in the WRF-STILT modelling. For the STILT simulations, 1000 particles are released and transported backward for up to 3 days with a temporal resolution of 1 h. Simply, the WRF

simulations provide the hourly meteorology, which further drives the STILT simulation to obtain the particle trajectory and footprint (f) within the study region. Similar to the spatial resolution set by WRF-STILT, the spatial resolution for the footprints is 3 km × 3 km. After obtaining the footprints, we calculate the model simulated CO mass concentration contributed from local emissions by multiplying a footprint by the corresponding *a priori* emission map (F) using the same method as discussed by Zhao et al. (2009),

$$C_l(X_r, t_r) = \sum_{i,j,m} f\left(X_r, t_r \middle| x_i, y_j, t_m\right) \cdot F\left(x_i, y_j\right) \quad (1)$$

where X_r and t_r represent the position and time of the CO measurement at the receptor location, respectively, $f(X_r, t_r | x_i, y_j, t_m)$ is the footprint, and $F(x_i, y_j)$ is the surface-emission map at position (x_i, y_j) and time t_m.

Fig. 2 provides a diagram describing how upstream air pollution and local emissions influence the corresponding air pollutant
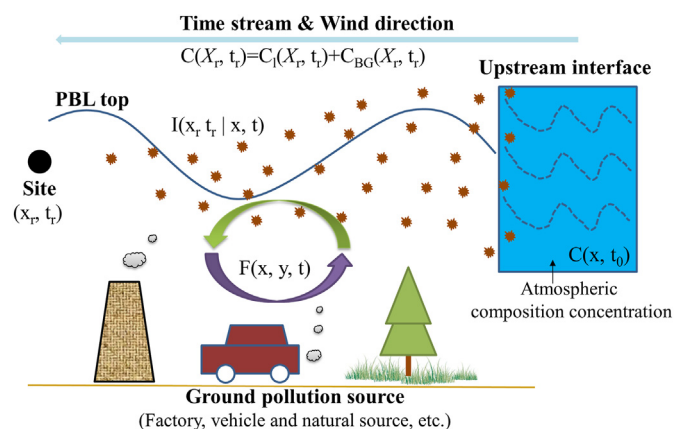

Fig. 2. The diagram of how upstream air pollution and local emissions influence the corresponding air pollutant measurements at the observation location (receptor).

measurements at the observation location (receptor). The transport process of an air parcel (or particles) includes two physical processes, advection and turbulence. The turbulence causes the dispersion of the air parcel (or particles) and promotes the exchange of gases or particles with the emissions from the surface. In principle, the observation gas concentration, such as the CO concentration, at the receptor location is a sum of the transported gas from upstream and the gas exchanged from the local surface emissions. Thus, the CO concentration at the receptor location can be calculated using the following equation:

$$C(X_r, t_r) = C_l(X_r, t_r) + C_{BG}(X_r, t_r) \qquad (2)$$

where C is the CO concentration at the receptor location, C_l is the CO concentration contributed from the exchange with the local surface emissions along the transport path, and C_{BG} is the CO concentration of the upstream atmosphere. Considering the much weaker footprints at farther locations, the very small CO concentration from the natural background, and the relatively long period (three days) of the backward trajectories, we simply assume the C_{BG} as a negligible component in our study. Note that if C_{BG} is non-zero, then the estimated enhancements (C-C_{BG}) will be lower and additional uncertainties could be introduced; however, we expect C_{BG} to be weak, as argued above. Eq. (2) is the basis for the derivation of the CO concentration at the receptor location from the WRF-STILT model.

2.5. Inversion technique

Fig. S1 shows the framework of how we retrieve the local emissions based on the WRF-STILT simulations and the site observations of CO concentration. In principle, the inversion algorithm is an optimal process: it estimates optimal emission scaling factors for the emissions in different sub-regions to make the WRF-STILT-based model calculations (section 2.4) closely match the site observations. In this study, we use the standard least-squares optimization method to estimate the overall scaling factor of each sub-region month by month.

Combining Eqs. (1) and (2), we can obtain

$$C = fF + C_{BG} \qquad (3)$$

where f is the footprint, F is the surface-emission map of CO, and C and C_{BG} are the CO mixing ratios at the receptor location and upstream location (background), respectively. Similar to Zhao et al. (2009), we introduce λ as scaling factors to the a priori emissions over all sub-regions within the study area, which is obtained from the optimal inversion process by comparing the model simulations and site observations. Unlike the approach used by Zhao et al. (2009), the standard least-squares optimization method is used to obtain the λ values:

$$\min\{abs(C_{obs} - f\phi\lambda)\} \qquad (4)$$

where Φ refers specifically to the a priori emissions from different sub-regions and C_{obs} refers to the observed CO concentration. After obtaining the optimal λ values, new surface emissions F (λ) can be obtained based on the multiplication of the a priori emissions over different sub-regions by its corresponding λ values:

$$F(\lambda) = \Phi\lambda \qquad (5)$$

We briefly summarize our analysis method shown in Fig. S1. We first derive reliable meteorology data from the WRF simulations. Second, we use the meteorology data to drive the STILT simulations and obtain the backward trajectories and footprints over the study

area. Third, based on the a priori CO emissions over the study area, we calculate the simulated CO concentration at the receptor (measurement) location. Fourth, we compare the simulated and measured CO concentrations and derive the scaling factors for CO emissions over selected sub-regions based on the standard least-squares optimization method. Fifth, after determining the scaling factors, we obtain the new optimal CO emission maps, run the models again to obtain new simulation results of CO concentration at the receptor location for other independent times, and evaluate their performance using CO measurements at those independent times.

Notably, large potential errors could exist due to the uncertainties in the meteorological variables such as the wind and planetary boundary layer, the transport model, and the a priori emission maps, as indicated by Zhao et al. (2009) in a CH_4 emission study. However, the purpose of this study is to provide a first estimate of CH_4 emissions with the constraint of CO concentration measurements over the Zhengzhou area, which can provide useful information for future research and air quality control policy making.

3. Results and discussion

3.1. Characteristics of CO observations

Fig. 3 shows the hourly (Fig. 3a) and monthly (Fig. 3b) variations in CO mass concentration along with its diurnal variation (Fig. 3c) from November 2017 to February 2018 measured at the Zhengzhou site. As shown in Fig. 3a, the CO concentration varies between 0 and 4 mg m^{-3} during the study period, peaking on January 20, 2018. The hourly variations in CO concentration are relatively weaker in November 2017 and February 2018 than in December 2017 and January 2018. By averaging the hourly CO concentration in each month (Fig. 3b), the maximum monthly CO concentration also peaks in January 2018 at a value of 1.27 mg m^{-3}. In contrast, the minimum monthly average CO concentration was in November 2017, which could be related to winter heating from November 15 until the 15th of the next March.

Fig. 3c shows the diurnal variation in the four-month averaged CO concentration. There is a clear diurnal variation in CO concentration in Zhengzhou in the winter of 2017, which is consistent with previous studies (Amorim et al., 2016; Hernández-Paniagua et al., 2018). There are two periods of rapidly increasing CO concentration in Zhengzhou, which are from 06:00 to 09:00 and from 16:00 to 20:00. This should be mainly due to the exhaust emissions from motor vehicles during morning and evening traffic peaks in the city. In contrast, there is a period of rapidly decreasing CO concentration from 9:00 to 16:00, which should be mainly due to the increasing planetary boundary layer (PBL) height. The weak change in CO concentration at night is likely associated with low emissions and relatively stable PBL height (Gratsea et al., 2017; Han et al., 2018; Hernández-Paniagua et al., 2018).

3.2. Footprints

Fig. 4 shows the average footprint map over the Zhengzhou area obtained from the WRF-STILT simulations, which represent the influencing factor of surface emissions on the measurement site (receptor) location. The footprint map shows a distinct spatial distribution, with large values in the northeast and northwest representing more contributions from those areas. This distribution is closely related to the geographical location of the study area and the wind characteristics in winter over the Zhengzhou area. As indicated by previous studies (Liu et al., 2018b; Wang et al., 2018), the wind in Zhengzhou is mainly from the north in winter.
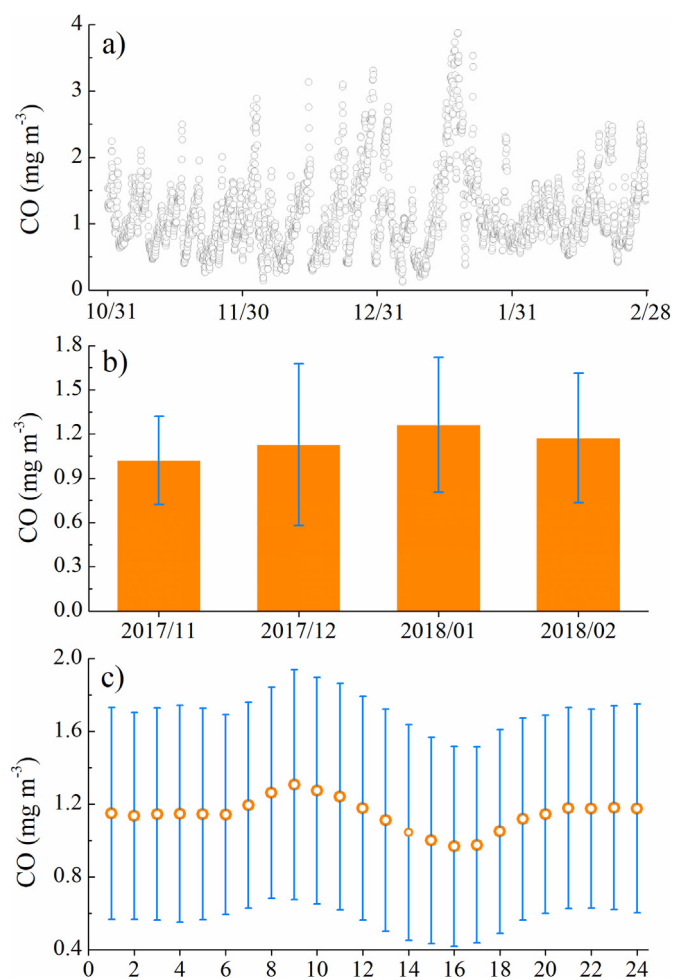
Fig. 3. The hourly (a) and monthly (b) variations in CO concentration along with its diurnal variation (c) measured at the site. The error bars in (b) and (c) represent the standard deviation.
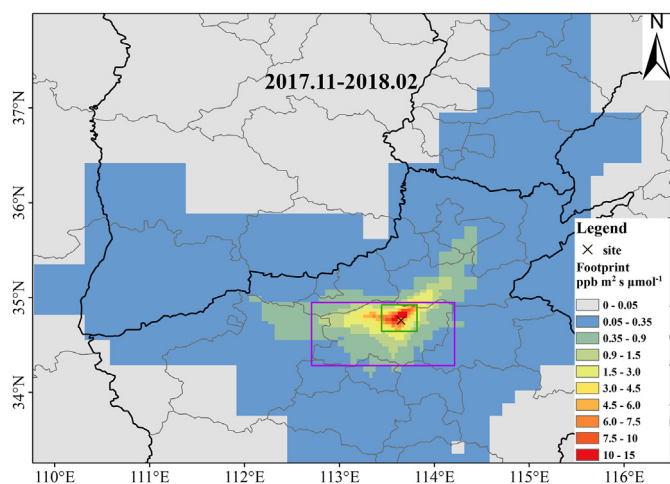

Fig. 4. The average footprints of November 2017 to February 2018. "x" denotes the receptor location. The purple box approximately represents the Zhengzhou city area, and the green box indicates the Zhengzhou city centre. (For interpretation of the references to colour in this figure legend, the reader is referred to the Web version of this article.)
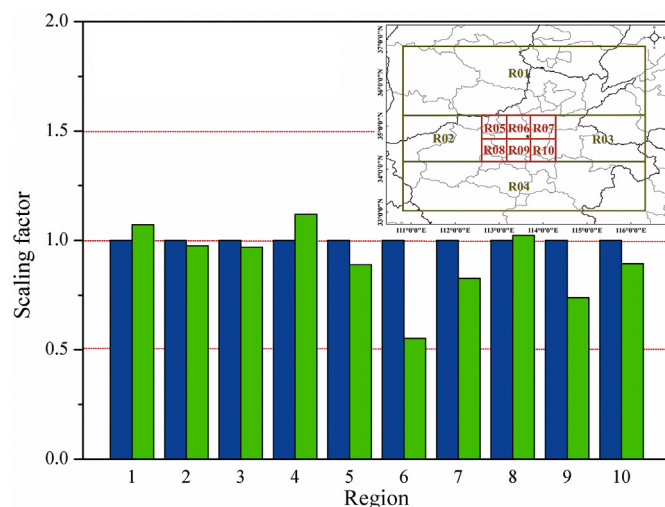

Fig. 5. The division of 10 sub-regions in the Zhengzhou study area along with the optimal scaling factors (green bars) over the 10 sub-regions from the inverse based on CO measurements from November 2017 to February 2018. The blue colour bars represent the *a priori* scaling factors, which are set to 1.0 for all the sub-regions. (For interpretation of the references to colour in this figure legend, the reader is referred to the Web version of this article.)

Moreover, Fig. 1 shows that the Taihang Mountains, low North China Plain, and narrow Fenwei Plain are in the northern, eastern/northeastern, and western parts of Zhengzhou, respectively. This topography promotes the transport of air pollutants from the northeast and northwest. Considering the heavily polluted areas of North China in the northeast of Zhengzhou and the Fenwei Plain in the western part of Zhengzhou, the air quality over Zhengzhou could be highly influenced by emissions from the northeast and northwest. In addition, air pollutant emissions are also significant over the southern part of Zhengzhou, which is a plain area with a high population. In short, the pollution contribution from emissions over the surrounding regions, such as the northeast and northwest study area, may not be ignored, while the footprints there seem very low compared to Zhengzhou area, as shown in Fig. 4.

As indicated in Zhao et al. (2009), the footprints indicate the influence factor of unit emission at each region on the CO concentration measurements at the observation (receptor) site location. The green box in Fig. 4 represents the built-up area of Zhengzhou city centre, and the purple box represents Zhengzhou and its surrounding county areas. Fig. S2 further shows the spatial distribution of land use in Zhengzhou in 2018, from which we can see that the urban area over Zhengzhou is the area with high footprints, as shown in Fig. 4, with the exception of the southwestern mountain region. Thus, the contributions to CO measurements at the observation site from the local emissions should be more significant than those from transport from outside the Zhengzhou area. Considering that the topography over Zhengzhou is relatively flat with high footprints, it is key to control the local emissions to improve the air quality in Zhengzhou (Fan et al., 2018; Kang et al., 2019; Liu et al., 2019b; Zhao et al., 2019). We next derive the optimal emissions from the site observations of CO concentration and the footprints from the WRF-STILT simulations.

3.3. Inversion analysis

Overall, Fig. 5 shows that the scaling factors for the optimal emissions are on average lower than 1.0, indicating that the CO emission amount is less than the inventory values for most sub-

regions. Particularly, the scaling factors for sub-regions 5, 6, 7, 9, and 10 are relatively low, with values of 0.87, 0.53, 0.85, 0.75 and 0.90, respectively, suggesting that the optimal emissions are less than the inventory emissions from the MEIC in these five regions. Note that the footprints are most distinct in these five regions, as shown in Fig. 4, suggesting that the inverse values in these five regions are generally more reliable than in other regions (Zhao et al., 2009). In contrast, the scaling factors in sub-regions 1 and 4 are 1.07 and 1.12, respectively, which are slightly larger than 1, indicating that the posterior/optimal emissions are likely slightly greater than the *a priori* estimations. For regions 2, 3, and 8, the scaling factors are closer to 1, which either suggests that the *a priori* CO emissions are reasonable or suggests the low sensitivity (footprints) of the CO observations at the measurement site to the emissions at these regions. While not provided in Fig. 5, the absolute CO emission amounts from regions 1−10 of the *a priori* emission map are 5.86, 0.87, 1.19, 3.06, 0.67, 0.79, 0.32, 0.15, 0.11, and 0.13 Mt/year, respectively.

As shown in Fig. 6a, the best-fitting linear regression equation between the WRF-STILT simulations of CO concentration (y) using the *a priori* emissions and the CO measurements (x) is y = 0.45x + 0.92 with a coefficient of determination of only 0.07, suggesting large uncertainties in the *a priori* emissions. Using the optimal scaling factors, the WRF-STIT simulations of CO concentration agree more closely with the CO measurements with the linear fitting regression equation y = 0.87x + 0.15 and the coefficient of determination of 0.48, which are shown in Fig. 6b. The results shown in Fig. 6 indicate that the new optimal emissions derived with the scaling factors could better represent the real emission conditions than the *a priori* emissions if the WRF-STILT model is assumed to be reliable.

We further performed inverse analyses on a monthly basis. Two observations can be clearly made from Fig. 7. First, the monthly average CO concentration from the WRF-STILT simulations with the optimal emissions agrees more closely with the observations than that from the WRF-STILT simulations with the *a priori* emissions. Second, the major ranges from the lower quartile or lower 5% to the upper quartile or upper 95% for the monthly CO concentrations
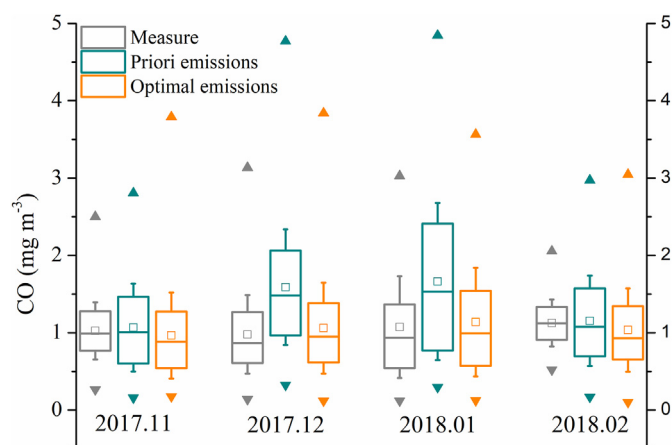

Fig. 7. The box plots of monthly CO concentrations from the observations, WRF-STILT simulations based on the *a priori* emissions, and WRF-STILT simulations based on the optimal emissions. The box indicates the median, upper and lower quantiles. In the box plot, an open square represent a mean, and the up and down triangles represent the maximum and minimum values, respectively. The whisker represents the 5%−95% range of the data.

from the WRF-STILT simulations with the optimal emissions also agree more closely with the observations than those from the WRF-STILT simulations with the *a priori* emissions. Particularly, the agreement of the CO concentrations between the WRF-STILT simulations and site observations in December and January considering the optimal emissions are significantly improved over those considering the *a priori* emissions. In addition, it is clear that the diurnal variation in CO concentrations from the WRF-STILT simulations using the optimal emissions agrees more closely with the observations than that from the WRF-STILT simulations using the *a priori* emissions (Fig. 8). In principle, the WRF-STILT-simulated CO concentration using the *a priori* emissions hardly captures the increasing trend from 07:00 to 10:00 and the decreasing trend from 10:00 to 17:00, while the WRF-STILT-simulated CO concentration determined using the optimal emissions can.
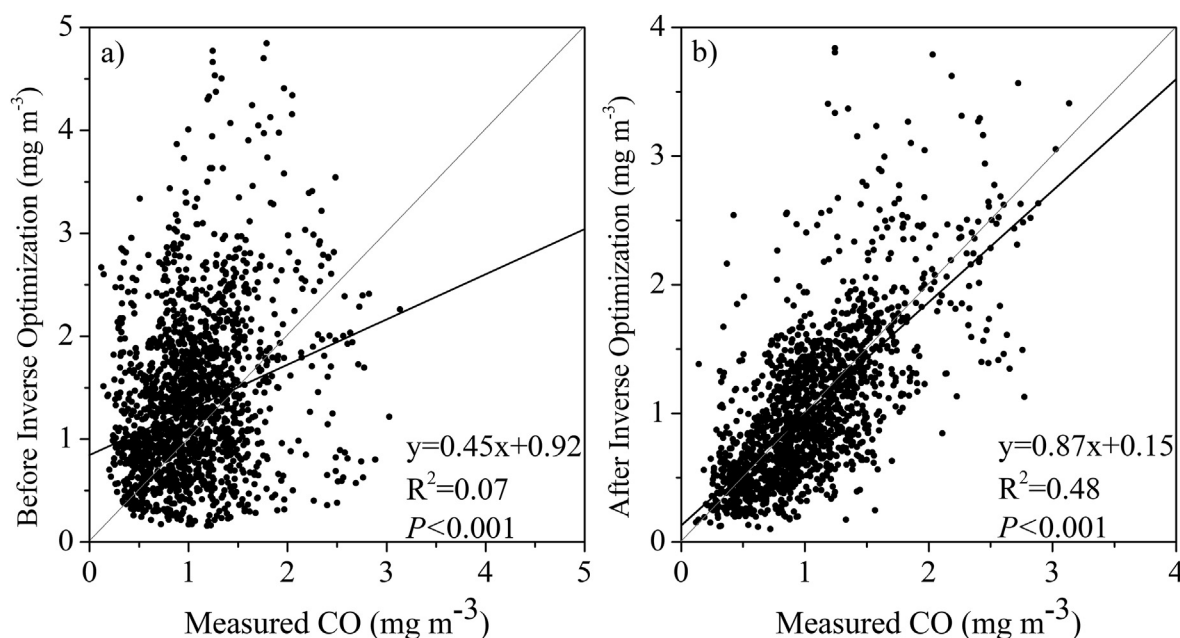

Fig. 6. Comparison of CO concentration between the measurements and predictions modified using scaling factors obtained from the inversion analysis.
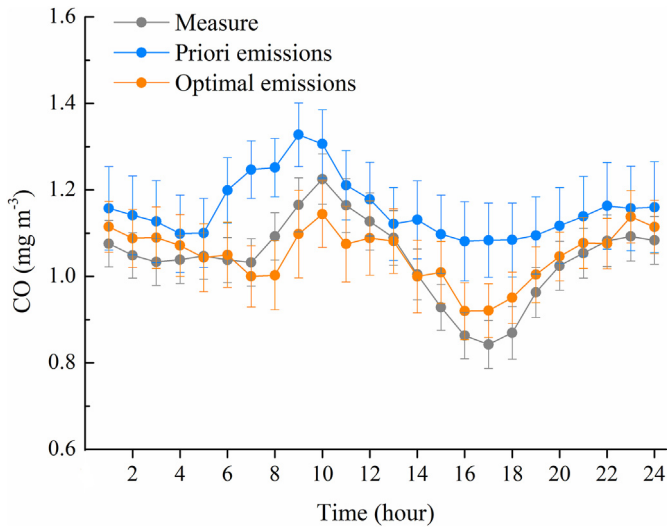
Fig. 8. Diurnal variations in CO concentrations from measurements (grey), WRF–STILT simulations based on the *a priori* emissions (blue), and WRF–STILT simulations based on the optimal emissions (orange). Circles represent the mean values, and the error bars represent the standard errors. (For interpretation of the references to colour in this figure legend, the reader is referred to the Web version of this article.)

We confirmed that the WRF-STILT-simulated CO concentrations determined using the optimal emissions agree more closely with the observations than those using the *a priori* emission for each month, also implying the high reliability of the new optimal CO emissions (Fig. 9). The slopes of the linear fitting regressions between the WRF-STILT-simulated CO concentrations determined using the optimal emissions and the observations range from 0.72 to 0.89 for four months, and all the fitting results passed the significance test (P < 0.001). All the results shown in Figs. 6–9 indicate that the inverse optimization method we used can significantly improve the estimates of CO emissions and make the predicted CO signals more consistent with the measured CO signals.

We then used the data from November 2017 to January 2018 to obtain the scaling factors and then used the scaling factors to optimize the inventory emissions for February 2018, based on which we conducted an independent evaluation study by comparing the WRF-STILT simulations and measurements of CO concentration in February 2018. As shown in Table S1, the WRF-STILT-simulated CO concentrations determined using the optimal emissions are much closer to the measurements in terms of both the mean and standard deviation compared to those from the WRF-STILT simulations using the *a priori* emissions. Simultaneously, compared to the WRF-STILT-simulated CO concentrations determined using the *a priori* emissions, the WRF-STILT-simulated CO
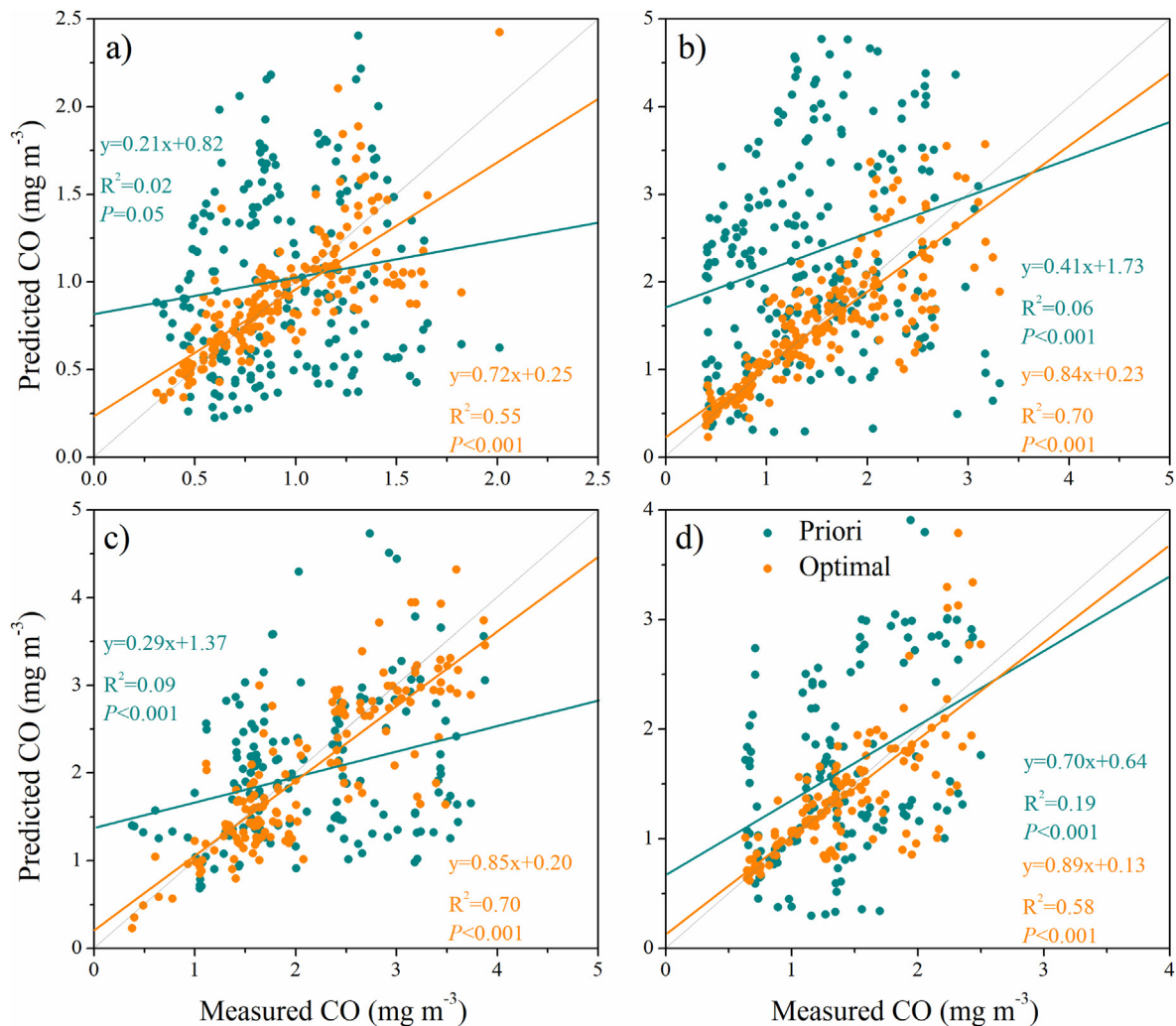

Fig. 9. Comparison of CO concentration between the measurements and predictions modified using the monthly scaling factors obtained from the inversion analysis. (a), (b), (c), and (d) represent November 2017, December 2017, January 2018, and February 2018, respectively.

concentrations determined using the optimal emissions agree more closely with the CO measurements, with a linear fitting regression equation of y = 0.84x + 0.11 and an R^2 of 0.46 (P < 0.001). This independent evaluation analysis further ensures the reliability of CO emission estimates from the optimal inversion study.

4. Conclusion

This study found that the CO concentration at Zhengzhou shows clear hourly and monthly variations in winter, along with significant diurnal variations. The temporal and diurnal variations in CO concentration are highly related to the local emissions, such as the heavier emissions in the heating season from November 15 to March 15, while the transport of air pollutants from northeast and northwest Zhengzhou also contributes.

An inverse algorithm is developed to estimate the optimal CO emissions over 10 classified sub-regions. We first performed the analysis for the whole study period. The optimal scaling factors are clearly less than 1.0 for the central four regions, implying that the *a priori* inventory CO emissions could have been overestimated. Further comparison indicated that the WRF-STILT-simulated CO concentrations determined using the optimal emissions agree more closely with the observations than the WRF-STILT-simulated CO concentrations determined using the *a priori* emissions. When we applied the inverse algorithm to the CO concentration measurements from every month, the results showed a stronger agreement of the CO concentrations between the WRF-STILT-simulated CO concentrations determined simulations using the optimal emissions and the measurements than that between the WRF-STILT-simulated CO concentrations determined simulations using the *a priori* emissions and the measurements for all the months. Therefore, one implication of our study is that the inverse optimization method can significantly improve estimates of CO emissions and make the predicted CO signals more consistent with the measured ones. This study provides the community with an efficient method to derive optimal emission information for various air pollutants.

Author statement

Hao Fan: Visualization, Data curation, Writing - Original draft preparation, Methodology, Software. **Chuanfeng Zhao**: Conceptualization, Investigation, Wring - Review & Editing, Supervision. **Zhanshan Ma**: Data curation, Investigation. **Yikun Yang**: Validation, Investigation.

Declaration of competing interest

The authors declare that they have no known competing financial interests or personal relationships that could have appeared to influence the work reported in this paper.

Acknowledgements

Appendix A. Supplementary data

Supplementary data to this article can be found online at https://doi.org/10.1016/j.envpol.2020.115164.

References

Amorim, J.H., Valente, J., Cascão, P., Ribeiro, L.M., Viegas, D.X., Ottmar, R., Miranda, A.I., 2016. Near-source grid-based measurement of CO and $PM_{2.5}$ concentration during a full-scale fire experiment in southern European shrubland, Atmos. Environ. Times 145, 19–28. https://doi.org/10.1016/j.atmosenv.2016.09.017.

Brophy, K., Graven, H., Manning, A.J., White, E., Arnold, T., Fischer, M.L., Jeong, S., Cui, X., Rigby, M., 2019. Characterizing uncertainties in atmospheric inversions of fossil fuel CO_2 emissions in California. Atmos. Chem. Phys. 19 (5), 2991–3006. https://doi.org/10.5194/acp-19-2991-2019.

Che, W.W., Frey, H.C., Lau, A.K., 2016. Sequential measurement of intermodal variability in public transportation $PM_{2.5}$ and CO exposure concentrations. Environ. Sci. Technol. 50 (16), 8760–8769. https://doi.org/10.1021/acs.est.6b01594.

Choi, H.-D., Liu, H.Y., Crawford, J.H., Considine, D.B., Allen, D.J., Duncan, B.N., Horowitz, L.W., Rodriguez, J.M., Strahan, S.E., Zhang, L., Liu, X., Damon, M.R., Steenrod, S.D., 2017. Global O_3−CO correlations in a chemistry and transport model during July−August: evaluation with TES satellite observations and sensitivity to input meteorological data and emissions. Atmos. Chem. Phys. 17 (13), 8429–8452. https://doi.org/10.5194/acp-17-8429-2017.

CSY, 2018. China Statistical Yearbook. China Statistical Publishing House, Beijing.

Cui, X.G., Newman, S., Xu, X.M., Andrews, A.E., Miller, J., Lehman, S., Jeong, S., Zhang, J.S., Priest, C., Campos-Pineda, M., Gurney, K.R., Graven, H., Southon, J., Fischer, M.L., 2019. Atmospheric observation-based estimation of fossil fuel CO_2 emissions from regions of central and southern California. Sci. Total Environ. 664, 381–391. https://doi.org/10.1016/j.scitotenv.2019.01.081.

Cusworth, D.H., Jacob, D.J., Sheng, J.-X., Benmergui, J., Turner, A.J., Brandman, J., White, L., Randles, C.A., 2018. Detecting high-emitting methane sources in oil/gas fields using satellite observations. Atmos. Chem. Phys. 18 (23), 16885–16896. https://doi.org/10.5194/acp-18-16885-2018.

Dekker, I.N., Houweling, S., Aben, I., Röckmann, T., Krol, M., Martínez-Alonso, S., Deeter, M.N., Worden, H.M., 2017. Quantification of CO emissions from the city of Madrid using MOPITT satellite retrievals and WRF simulations. Atmos. Chem. Phys. 17 (23), 14675–14694. https://doi.org/10.5194/acp-17-14675-2017.

Dekker, I.N., Houweling, S., Pandey, S., Krol, M., Röckmann, T., Borsdorff, T., Landgraf, J., Aben, I., 2019. What caused the extreme CO concentrations during the 2017 high-pollution episode in India? Atmos. Chem. Phys. 19 (6), 3433–3445. https://doi.org/10.5194/acp-19-3433-2019.

Fan, T.Y., Liu, X.H., Ma, P.-L., Zhang, Q., Li, Z.Q., Jiang, Y.Q., Zhang, F., Zhao, C.F., Yang, X., Wu, F., Wang, Y.Y., 2018. Emission or atmospheric processes? An attempt to attribute the source of large bias of aerosols in eastern China simulated by global climate models. Atmos. Chem. Phys. 18 (2), 1395–1417. https://doi.org/10.5194/acp-18-1395-2018.

Feng, S.Z., Jiang, F., Wu, Z., Wang, H.M., Ju, W.M., Wang, H.K., 2020. CO emissions inferred from surface CO observations over China in December 2013 and 2017. J. Geophys. Res. Atmos. 125 https://doi.org/10.1029/2019JD031808.

Garrett, T.J., Zhao, C., Noel, P.C., 2010. Assessing the relative contributions of transport efficiency and scavenging to seasonal variability in Arctic aerosol. Tellus B 62, 190–196. https://doi.org/10.1111/j.1600-0889.2010.00453.x.

Girach, I.A., Ojha, N., Nair, P.R., Pozzer, A., Tiwari, Y.K., Kumar, K.R., Lelieveld, J., 2017. Variations in O_3, CO, and CH_4 over the Bay of Bengal during the summer monsoon season: shipborne measurements and model simulations. Atmos. Chem. Phys. 17 (1), 257–275. https://doi.org/10.5194/acp-17-257-2017.

Gratsea, M., Liakakou, E., Mihalopoulos, N., Adamopoulos, A., Tsilibari, E., Gerasopoulos, E., 2017. The combined effect of reduced fossil fuel consumption and increasing biomass combustion on Athens' air quality, as inferred from long term CO measurements. Sci. Total Environ. 592, 115–123. https://doi.org/10.1016/j.scitotenv.2017.03.045.

Han, H., Liu, J., Yuan, H., Jiang, F., Zhu, Y., Wu, Y., Wang, T., Zhuang, B., 2018. Impacts of synoptic weather patterns and their persistence on free tropospheric carbon monoxide concentrations and outflow in eastern China. J. Geophys. Res. Atmos. 123 (13), 7024–7046. https://doi.org/10.1029/2017jd028172.

Hassler, B., McDonald, B.C., Frost, G.J., Borbon, A., Carslaw, D.C., Civerolo, K., Granier, C., Monks, P.S., Monks, S., Parrish, D.D., Pollack, I.B., Rosenlof, K.H., Ryerson, T.B., von Schneidemesser, E., Trainer, M., 2016. Analysis of long-term observations of NOx and CO in megacities and application to constraining emissions inventories. Geophys. Res. Lett. 43 (18), 9920–9930. https://doi.org/10.1002/2016gl069894.

Hernández-Paniagua, I.Y., Lowry, D., Clemitshaw, K.C., Palmer, P.I., Fisher, R.E., France, J.L., Mendoza, A., O'Doherty, S., Forster, G., Lanoiselle, M., Nisbet, E.G., 2018. Diurnal, seasonal, and annual trends in tropospheric CO in Southwest London during 2000−2015: wind sector analysis and comparisons with urban and remote sites. Atmos. Environ. 177, 262–274. https://doi.org/10.1016/j.atmosenv.2018.01.027.

Holloway, T., Levy, H., Kasibhatla, P., 2000. Global distribution of carbon monoxide. J. Geophys. Res. Atmos. 105 (D10), 12123–12147. https://doi.org/10.1029/1999jd901173.

Hu, C., Griffis, T.J., Lee, X., Millet, D.B., Chen, Z., Baker, J.M., Xiao, K., 2018. Top-down constraints on anthropogenic CO₂ emissions within an agricultural-urban landscape. J. Geophys. Res. Atmos. 123 (9), 4674–4694. https://doi.org/10.1029/2017jd027881.

Hu, C., Griffis, T.J., Liu, S., Xiao, W., Hu, N., Huang, W., Yang, D., Lee, X., 2019. Anthropogenic methane emission and its partitioning for the yangtze river delta region of China. J. Geophys. Res.-Biogeo. 124 (5), 1148–1170. https://doi.org/10.1029/2018jg004850.

Jeong, S., Newman, S., Zhang, J.S., Andrews, A.E., Bianco, L., Bagley, J., Cui, X.G., Graven, H., Kim, J., Salameh, P., LaFranchi, B.W., Priest, C., Campos-Pineda, M., Novakovskaia, E., Sloop, C.D., Michelsen, H.A., Bambha, R.P., Weiss, R.F., Keeling, R., Fischer, M.L., 2016. Estimating methane emissions in California's urban and rural regions using multitower observations. J. Geophys. Res. Atmos. 121 (21) https://doi.org/10.1002/2016jd025404, 13,031-013,049.

Jeong, S., Zhao, C.F., Andrews, A.E., Bianco, L., Wilczak, J.M., Fischer, M.L., 2012a. Seasonal variation of CH₄ emissions from central California. J. Geophys. Res. Atmos. 117 (D11) https://doi.org/10.1029/2011jd016896.

Jeong, S., Zhao, C.F., Andrews, A.E., Dlugokencky, E.J., Sweeney, C., Bianco, L., Wilczak, J.M., Fischer, M.L., 2012b. Seasonal variations in N₂O emissions from central California. Geophys. Res. Lett. 39 (16) https://doi.org/10.1029/2012gl052307.

Jiang, Z., Jones, D.B.A., Worden, H.M., Henze, D.K., 2015a. Sensitivity of top-down CO source estimates to the modeled vertical structure in atmospheric CO. Atmos. Chem. Phys. 15 (3), 1521–1537. https://doi.org/10.5194/acp-15-1521-2015.

Jiang, Z., Jones, D.B.A., Worden, J., Worden, H.M., Henze, D.K., Wang, Y.X., 2015b. Regional data assimilation of multi-spectral MOPITT observations of CO over North America. Atmos. Chem. Phys. 15 (12), 6801–6814. https://doi.org/10.5194/acp-15-6801-2015.

Jiang, Z., Worden, J.R., Worden, H., Deeter, M., Jones, D.B.A., Arellano, A.F., Henze, D.K., 2017. A 15-year record of CO emissions constrained by MOPITT CO observations, Atmos. Chem. Phys. 17 (7), 4565–4583. https://doi.org/10.5194/acp-17-4565-2017.

Kang, H., Zhu, B., van der A, R.J., Zhu, C., de Leeuw, G., Hou, X., Gao, J., 2019. Natural and anthropogenic contributions to long-term variations of SO₂, NO₂, CO, and AOD over East China. Atmos. Res. 215, 284–293. https://doi.org/10.1016/j.atmosres.2018.09.012.

Khan, A., Szulejko, J.E., Bae, M.S., Shon, Z.H., Sohn, J.-R., Seo, J.W., Jeon, E.C., Kim, K.-H., 2017. Long-term trend analysis of CO in the Yongsan district of Seoul, Korea, between the years 1987 and 2013. Atmos. Pollut. Res. 8 (5), 988–996. https://doi.org/10.1016/j.apr.2017.03.006.

Li, L., Liu, Y., 2011. Space-borne and ground observations of the characteristics of CO pollution in Beijing, 2000–2010, Atmos. Environ. Times 45 (14), 2367–2372. https://doi.org/10.1016/j.atmosenv.2011.02.026.

Li, M., Zhang, Q., Streets, D.G., He, K.B., Cheng, Y.F., Emmons, L.K., Huo, H., Kang, S.C., Lu, Z., Shao, M., Su, H., Yu, X., Zhang, Y., 2014. Mapping Asian anthropogenic emissions of non-methane volatile organic compounds to multiple chemical mechanisms. Atmos. Chem. Phys. 14, 5617–5638. https://doi.org/10.5194/acp-14-5617-2014.

Lin, J.C., Gerbig, C., Wofsy, S.C., Andrews, A.E., Daube, B.C., Davis, K.J., 2003. A near-field tool for simulating the upstream influence of atmospheric observations: the Stochastic Time-Inverted Lagrangian Transport (STILT) model. J. Geophys. Res. Atmos. 108 (D16) https://doi.org/10.1029/2002jd003161.

Liu, C., Yin, P., Chen, R.J., Meng, X., Wang, L.J., Niu, Y., Lin, Z.J., Liu, Y.N., Liu, J.M., Qi, J.L., You, J.L., Kan, H.D., Zhou, M.G., 2018a. Ambient carbon monoxide and cardiovascular mortality: a nationwide time-series analysis in 272 cities in China. Lancet. Planet. Health. 2 (1), e12–e18. https://doi.org/10.1016/s2542-5196(17)30181-x.

Liu, S., Hua, S.B., Wang, K., Qiu, P.P., Liu, H.J., Wu, B.B., Shao, P.Y., Liu, X.Y., Wu, Y.M., Xue, Y.F., Hao, Y., Tian, H.Z., 2018b. Spatial-temporal variation characteristics of air pollution in Henan of China: localized emission inventory, WRF/Chem simulations and potential source contribution analysis. Sci. Total Environ. 624, 396–406. https://doi.org/10.1016/j.scitotenv.2017.12.102.

Liu, F., Zhang, Q., Tong, D., Zheng, B., Li, M., Huo, H., He, K.B., 2015. High-resolution inventory of technologies, activities, and emissions of coal-fired power plants in China from 1990 to 2010. Atmos. Chem. Phys. 15, 13299–13317. https://doi.org/10.5194/acp-15-13299-2015.

Liu, S., Fang, S.X., Liang, M., Sun, W.Q., Feng, Z.Z., 2019a. Temporal patterns and source regions of atmospheric carbon monoxide at two background stations in China. Atmos. Res. 220, 169–180. https://doi.org/10.1016/j.atmosres.2019.01.017.

Liu, X.Y., He, K.B., Zhang, Q., Lu, Z.F., Wang, S.W., Zhang, Y.X., Streets, D.G., 2019b. Analysis of the origins of black carbon and carbon monoxide transported to Beijing, Tianjin, and Hebei in China. Sci. Total Environ. 653, 1364–1376. https://doi.org/10.1016/j.scitotenv.2018.09.274.

Mallia, D.V., Lin, J.C., Urbanski, S., Ehleringer, J., Nehrkorn, T., 2015. Impacts of up-wind wildfire emissions on CO, CO₂, and PM₂.₅ concentrations in Salt Lake City, Utah. J. Geophys. Res. Atmos. 120 (1), 147–166. https://doi.org/10.1002/2014JD022472.

Marey, H.S., Hashisho, Z., Fu, L., Gille, J., 2015. Spatial and temporal variation in CO over Alberta using measurements from satellites, aircraft, and ground stations. Atmos. Chem. Phys. 15 (7), 3893–3908. https://doi.org/10.5194/acp-15-3893-2015.

Nehrkorn, T., Eluszkiewicz, J., Wofsy, S.C., Lin, J.C., Gerbig, C., Longo, M., Freitas, S., 2010. Coupled weather research and forecasting–stochastic time-inverted Lagrangian transport (WRF–STILT) model. Meteorol. Atmos. Phys. 107 (1–2), 51–64. https://doi.org/10.1007/s00703-010-0068-x.

Pal, S., Lee, T.R., De Wekker, S.F.J., 2017. A study of the combined impact of boundary layer height and near-surface meteorology on the CO diurnal cycle at a low mountaintop site using simultaneous lidar and in-situ measurements. Atmos. Environ. Times 164, 165–179. https://doi.org/10.1016/j.atmosenv.2017.05.041.

Petetin, H., Sauvage, B., Smit, H.G.J., Gheusi, F., Lohou, F., Blot, R., Clark, H., Athier, G., Boulanger, D., Cousin, J.-M., Nedelec, P., Neis, P., Rohs, S., Thouret, V., 2018. A climatological view of the vertical stratification of RH, O₃ and CO within the PBL and at the interface with free troposphere as seen by IAGOS aircraft and ozonesondes at northern mid-latitudes over 1994–2016. Atmos. Chem. Phys. 18 (13), 9561–9581. https://doi.org/10.5194/acp-18-9561-2018.

Saikawa, E., Kim, H., Zhong, M., Avramov, A., Zhao, Y., Janssens-Maenhout, G., Kurokawa, J.-i., Klimont, Z., Wagner, F., Naik, V., Horowitz, L.W., Zhang, Q., 2017. Comparison of emissions inventories of anthropogenic air pollutants and greenhouse gases in China. Atmos. Chem. Phys. 17 (10), 6393–6421. https://doi.org/10.5194/acp-17-6393-2017.

Singh, D., Kumar, A., Kumar, K., Singh, B., Mina, U., Singh, B.B., Jain, V.K., 2016. Statistical modeling of O₃, NOₓ, CO, PM₂.₅, VOCs and noise levels in commercial complex and associated health risk assessment in an academic institution. Sci. Total Environ. 572, 586–594. https://doi.org/10.1016/j.scitotenv.2016.08.086.

Stocker, T.F., Qin, D., Plattner, G.-K., Tignor, M., Allen, S.K., Boschung, J., Nauels, A., Xia, Y., Bex, V., Midgley, P.M., 2013. Climate Change 2013: the Physical Science Basis. Contribution of Working Group I to the Fifth Assessment Report of the Intergovernmental Panel on Climate Change. Cambridge University Press, Cambridge, United Kingdom and New York, NY, USA, p. 1535.

Streets, D.G., Zhang, Q., Wang, L.T., He, K.B., Hao, J.M., Wu, Y., Tang, Y.H., Carmichael, G.R., 2006. Revisiting China's CO emissions after the Transport and Chemical Evolution over the Pacific (TRACE-P) mission: synthesis of inventories, atmospheric modeling, and observations. J. Geophys. Res. Atmos. 111 (D14) https://doi.org/10.1029/2006jd007118.

Sun, W., Shao, M., Granier, C., Liu, Y., Ye, C.S., Zheng, J.Y., 2018. Long-term trends of anthropogenic SO₂, NOₓ, CO, and NMVOCs emissions in China, earths. Future Times 6 (8), 1112–1133. https://doi.org/10.1029/2018ef000822.

Townsend, C.L., Maynard, R.I., 2002. Effects on health of prolonged exposure to low concentrations of carbon monoxide. Occup. Environ. Med. 59 (10), 708–711. https://doi.org/10.1136/oem.59.10.708.

Vandyck, T., Keramidas, K., Kitous, A., Spadaro, J.V., Van Dingenen, R., Holland, M., Saveyn, B., 2018. Air quality co-benefits for human health and agriculture counterbalance costs to meet Paris Agreement pledges. Nat. Commun. 9 (1), 4939. https://doi.org/10.1038/s41467-018-06885-9.

Wang, J.Q., Qu, W.J., Li, C., Zhao, C.H., Zhong, X., 2018. Spatial distribution of wintertime air pollution in major cities over eastern China: relationship with the evolution of trough, ridge and synoptic system over East Asia. Atmos. Res. 212, 186–201. https://doi.org/10.1016/j.atmosres.2018.05.013.

Wen, D., Lin, J.C., Millet, D.B., Stein, A.F., Draxler, R.R., 2012. A backward-time stochastic Lagrangian air quality model. Atmos. Environ. 54, 373–386. https://doi.org/10.1016/j.atmosenv.2012.02.042.

WHO, 1999. Environmental Health Criteria 213: Carbon Monoxide, second ed. Finland: World Health Organisation, Geneva.

Wu, D., Lin, J.C., Fasoli, B., Oda, T., Ye, X., Lauvaux, T., Yang, E.G., Kort, E.A., 2018. A Lagrangian approach towards extracting signals of urban CO₂ emissions from satellite observations of atmospheric column CO₂ (XCO₂): X-Stochastic Time-Inverted Lagrangian Transport model ("X-STILT v1"). Geosci. Model Dev. (GMD) 11 (12), 4843–4871. https://doi.org/10.5194/gmd-11-4843-2018.

Yin, Y., Chevallier, F., Ciais, P., Broquet, G., Fortems-Cheiney, A., Pison, I., Saunois, M., 2015. Decadal trends in global CO emissions as seen by MOPITT. Atmos. Chem. Phys. 15 (23), 13433–13451. https://doi.org/10.5194/acp-15-13433-2015.

Yue, T., Gao, X., Gao, J.J., Tong, Y.L., Wang, K., Zuo, P.L., Zhang, X.X., Tong, L., Wang, C.L., Xue, Y.F., 2018. Emission characteristics of NOₓ, CO, NH₃ and VOCs from gas-fired industrial boilers based on field measurements in Beijing city, China, Atmos. Environ. Times 184, 1–8. https://doi.org/10.1016/j.atmosenv.2018.04.022.

Zhang, Q., Streets, D.G., Carmichael, G.R., He, K.B., Huo, H., Kannari, A., Klimont, Z., Park, I.S., Reddy, S., Fu, J.S., Chen, D., Duan, L., Lei, Y., Wang, L.T., Yao, Z.L., 2009. Asian emissions in 2006 for the NASA INTEX-B mission. Atmos. Chem. Phys. 9, 5131–5153.

Zhao, C.F., Andrews, A.E., Bianco, L., Eluszkiewicz, J., Hirsch, A., MacDonald, C., Nehrkorn, T., Fischer, M.L., 2009. Atmospheric inverse estimates of methane emissions from Central California. J. Geophys. Res. Atmos. 114 (D16) https://doi.org/10.1029/2008jd011671.

Zhao, C.F., Wang, Y., Shi, X.Q., Zhang, D.Z., Wang, C.Y., Jiang, J.H., Zhang, Q., Fan, H., 2019. Estimating the contribution of local primary emissions to particulate pollution using high-density station observations. J. Geophys. Res. Atmos. 124 (3), 1648–1661. https://doi.org/10.1029/2018jd028888.

Zheng, B., Chevallier, F., Ciais, P., Yin, Y., Deeter, M.N., Worden, H.M., Wang, Y.L., Zhang, Q., He, K.B., 2018. Rapid decline in carbon monoxide emissions and export from East Asia between years 2005 and 2016. Environ. Res. Lett. 13 (4), 044007 https://doi.org/10.1088/1748-9326/aab2b3.

Zheng, B., Huo, H., Zhang, Q., Yao, Z.L., Wang, X.T., Yang, X.F., Liu, H., He, K.B., 2014. High-resolution mapping of vehicle emissions in China in 2008. Atmos. Chem. Phys. 14 (18), 9787–9805. https://doi.org/10.5194/acp-14-9787-2014.